IEEE Access
Multidisciplinary ⋮ Rapid Review ⋮ Open Access Journal

Received 28 April 2025, accepted 31 July 2025, date of publication 29 August 2025, date of current version 17 September 2025.
Digital Object Identifier 10.1109/ACCESS.2025.3604369

RESEARCH ARTICLE

Real-Time Vehicle Tracking Using Magnetic Field Fingerprinting

R. E. VAN RUITENBEEK AND S. BHULAI
Vrije Universiteit Amsterdam, 1081 HV Amsterdam, The Netherlands
Corresponding author: R. E. van Ruitenbeek (revanruitenbeek@gmail.com)

ABSTRACT This paper focuses on developing a vehicle tracking algorithm for vehicle inspection systems. Tracking small vehicle movements in small enclosed systems can be challenging, but offers tremendous benefits to optimize the camera capture moment. Therefore, we focus on locating the vehicle position to ensure that pictures can be taken with equal spacing, limiting the likelihood of missed damages and making it easier to compare different inspections. We propose the usage of sensor fusion between Magnetic Field sensors and Time-of-Flight Lidar sensors and develop a fingerprinting method that accurately tracks vehicle movement through the system. Unlike previous research, we developed a unique approach that does not require offline data collection, prior knowledge of the vehicle, or any sensors to be attached to the vehicles. Using sensor fusion, we establish the fingerprint in real-time to ensure that the system does not require storing and collecting fingerprints in a database. We benchmark the proposed solution against varying vehicle brands, models, and driving behavior. The findings highlight the algorithm's exceptional performance, which tracks vehicles with less than 0.32 sensor distances in accuracy, or almost 3 centimeters when 64 sensors are used. We show that the algorithm can scale in the number of sensors to improve tracking granularity, with almost no compromise on the algorithm's accuracy. By evaluating different driving scenarios, we show that the proposed algorithm is robust against different driving speeds, speed changes, and complete stops of the vehicle during the drive-through process. Even when vehicles change driving direction, the proposed system demonstrates the capability to track them effectively.

INDEX TERMS Damage inspection, fingerprinting, times-series matching, vehicle tracking.

I. INTRODUCTION

The automation of vehicle inspections has garnered significant attention in recent years, focusing predominantly on the development of computer vision models to enhance detection capabilities [1], [2], [3], [4], [5], [6], [7]. Despite extensive research on image quality and its impact on vehicle inspection quality, less emphasis has been placed on optimizing the specific segment of the vehicle to be captured in each image.

Researchers have highlighted the importance of camera angle and viewpoint in visual inspection systems, suggesting a shift towards multi-view damage inspection to address these challenges. However, existing multi-view systems, such as the one proposed by Stent et al. [8] Tang et al. [9] Ruitenbeek and Bhulai [10], capture images from different angles based on a time trigger mechanism. A time-based capturing system limits the control to ensure image overlap consistently between each consecutive picture. With this, the overlap between the images depends on a constant driving speed, which needs to be known upfront and held constant during the inspection. With this strong dependency on the driver, complete automation of vehicle inspections remains challenging. Moreover, we highlight in previous research that knowing the vehicle's precise location facilitates matching damages across different views and eliminating duplicate detections [10].

This study aims to improve vehicle position estimation within a drive-through visual inspection system. By leveraging position estimation, images can be captured based on the vehicle's location rather than a fixed time interval, enhancing consistency and ensuring that variations in driving behavior do not affect the number or quality of images. This

The associate editor coordinating the review of this manuscript and approving it for publication was Masood Ur-Rehman.

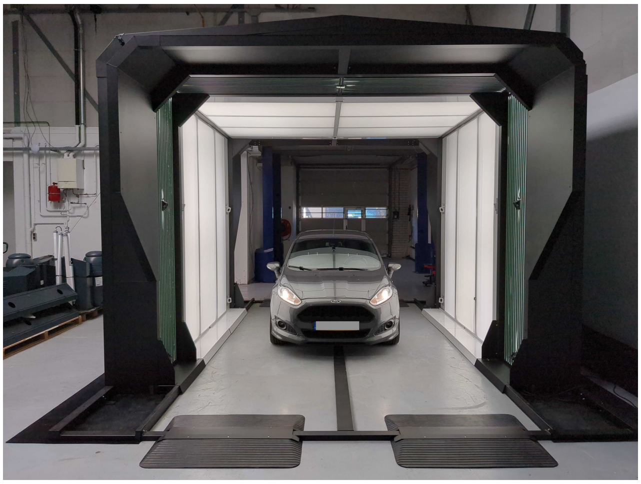

FIGURE 1. Drive-through vehicle inspection system which is completely enclosed to reduce influence from its surroundings.

consistency between images is particularly interesting when comparing multiple inspections to identify if damages are new or already known. Furthermore, a time-based system cannot accommodate vehicles that stop or change driving speed within the inspection area, necessitating a consistent speed during the inspection.

The objective of this chapter is to develop a precise vehicle tracking system for use within a vehicle inspection setup. A key challenge we face involves limitations on sensor usage due to environmental conditions. Previous studies, such as those conducted by Nassar et al. [11], De Deijn [3], and Ruitenbeek and Bhulai [7], have demonstrated that consistent lighting conditions significantly enhance image quality. To accommodate for this, we build upon our previously proposed multi-view inspection system [10] and use a fully enclosed inspection environment with a light diffuser to maintain uniform lighting on the vehicle. This setup is visualized in Figure 1.

Position estimation has been widely studied in fields such as automated driving, the railroad industry, and logistics. Techniques range from data-intensive methods like camera-based systems to the use of LIDARs, pressure sensors, and magnetic sensors. This study aims to track vehicles within a controlled, enclosed environment without prior knowledge of the vehicle or the option to attach additional sensors to it.

Although this research is centered around automated vehicle inspections, its implications extend beyond this domain. The global market for indoor positioning and navigation, valued at 6.1 billion in 2020, is projected to reach 17 billion by 2025 [12].

This research extends previous studies in three key ways. First, we introduce a hardware setup combined with an algorithm that leverages sensor fusion from Time-of-Flight (ToF) sensors and Magnetic Field (MF) sensors to estimate vehicle position using a fingerprinting approach. This technique maintains high inspection quality by adhering to restrictions on sensor placement within the system. Second, we demonstrate that our approach can accurately track vehicles throughout the system, regardless of their brand, model, or driving behavior. We show robustness against changes in driving speed, halting the vehicle during the inspection, and reversing the vehicle during the inspection. Third, unlike previous studies, our method does not require any prior information about the vehicle, nor does it necessitate attaching sensors to the vehicle itself. This is a significant improvement over previous approaches, such as those proposed by Farrell and Barth [13], Byun and Kim [14], Byun and Jeong [15], which suggested or implemented sensors attached to vehicles. Moreover, our proposed tracking algorithm constructs the fingerprint in real-time when the vehicle enters the tracking area. With this, we avoid the need to construct, store, and maintain fingerprints for all types of vehicles in a database, overcoming a large drawback of previous research [16], [17], [18], [19]. These considerations are crucial in addressing practical constraints, especially when the inspecting company does not own the vehicle fleet, making it impractical to install sensors on each vehicle.

II. RELATED WORK

The task of accurately determining object positions and tracking objects is a multifaceted problem that has obtained significant research interest. As technology has advanced, various methodologies have emerged, each with unique strengths and limitations. This chapter provides a review of the related work on object tracking, focusing on key approaches such as geometric localization, LIDAR-based systems, fingerprinting techniques, magnetic sensors, and visual-based methods.

Geometric approaches are frequently employed to locate objects in 3D space, with mobile phone localization being a notable application. Triangulation is a widely used geometric method for detecting mobile phone locations, utilizing Time of Arrival (ToA) or Received Signal Strength (RSS) measurements to perform the triangulation process [12]. The RSS combines the signal strength from three base stations to interpolate the approximate position. On the contrary, ToA focuses on the travel time of the signal instead of the signal strength itself.

Another approach, frequently used in indoor settings, is the use of Time-of-Flight (ToF) sensors. ToF sensors emit light and measure the time taken for the light to be transmitted, reflected off the object, and returned to the sensor. A localization method solely focused on ToF sensors has been proposed by [20]. The primary benefits of ToF sensors are their relatively low latency and rapid update rates [12]. However, a potential downside is the influence of the object's color and shape. Sharp angles on the target object can reflect the light away from the sensor, resulting in insufficient light being returned. Consequently, accurate distance estimation can be compromised.

A. FINGERPRINTING

Fingerprinting approaches to estimate object location gained popularity [12]. Fingerprinting involves creating an RSS pattern that stores the object's location along with the measurement output. These measurements are collected upfront in an offline environment, and the sensor outputs are then compared with new sensor measurements when localization needs to take place.

Despite their widespread use, Zafari et al. [21] argue that obtaining accurate locations is challenging due to sensor noise. The RSS pattern often degrades over time as environmental changes between the offline RSS creation and actual (online) tracking can affect accuracy [18]. Examples of such changes include moved objects, opened or closed doors, and variations in the number of people in the environment [12]. To mitigate some of this noise, Yang et al. [22] and Hellmers et al. [23] applied a Kalman Filter (KF) to the sensor data.

A successful example of fingerprinting is the implementation by Gansemer et al. [19], which used WLAN fingerprinting in combination with Euclidean Distance Algorithms to track people through buildings with an accuracy of 0.5 meters. Similarly, Koike-Akino et al. [16] implemented WLAN based tracking with 3 access points to obtain an RMSE below 12cm. Compared to most indoor localization systems, MF tracking systems are relatively cost- and energy-efficient [12]. Hellmers et al. [23] implemented MF tracking and achieved positioning accuracy in the range of 0.5 - 1.5 meters.

To date, most research on indoor localization systems has not utilized sensor fusion [12]. Employing complementary sensors often leads to improved positioning accuracy [24]. Du et al. [18] introduced a visual-based camera tracking system in combination with MF sensors, using the fingerprint approach. They compared new images of individuals with images in the database and used a similarity score to determine the most similar picture in terms of location. They demonstrated that this approach can enhance the MF method by more than 50%.

B. MAGNETIC SENSORS

Farrell and Barth [13] proposed a vehicle positioning method that combines GPS data with magnetic sensors mounted on the front and rear of the vehicle. This method estimates the absolute position using magnetic markers placed within the road. A similar approach, without GPS integration, is frequently used for guiding autonomous vehicles or robots in warehouses. Magnetic sensors combined with gyroscope and steering angle sensors are often used to achieve accurate localization [15]. The use of magnetic sensors, in conjunction with markers in the surrounding area, is a proven solution that requires low maintenance and no physical contact between the sensor and the object [25], [26], [27]. A significant advantage of this method is that glitter on the floor does not affect localization, unlike optical sensors. However, limitations of these systems include the sensor's sampling rate and the vehicle position calculation time, resulting in lower driving speeds to measure location accurately [15]. One major benefit of placing markers in the immediate vicinity is the clear Gaussian-shaped function that appears when the magnetic sensor moves over the magnetic marker.

Both Byun and Kim [14] and Byun and Jeong [15] mounted a series of magnetic sensors across the entire width of test vehicles with a spacing of 1 - 2 centimeters to obtain the Gaussian profile from multiple sensors. Detection, when the object is directly above the marker, is straightforwardly obtained by analyzing the differential of the Gaussian. Similarly, Trinh et al. [28] tracked objects in a relatively small square area of $400 cm^2$ by consulting the gradients of a single-dimension magnetic field. In a different approach, Caruso and Withanawasam [29] implemented a single three-axis Anisotropic Magneto Resistance (AMR) sensor to obtain the vehicle silhouette and use it to distinguish between cars, vans, trucks, buses, and trailers.

To track multiple moving targets, Wang et al. [30] implemented a magnetic force tracking algorithm designed for objects such as submarines. They utilized magnetic gradient tensors, a special type of magnetic sensor that suppresses time-domain interference [30]. Their study examined the effect of a moving detector on tracking multiple moving targets.

C. IMAGE-BASED OBJECT LOCALIZATION

Position estimation and movement tracking through computer vision have garnered significant interest over the past decade. However, these systems face challenges, particularly in handling occlusion, which can degrade the quality of localization and tracking efforts [31], [32], [33].

Visual methods are commonly employed to determine the spatial coordinates of objects. This typically involves using markers or landmarks visible to the camera as reference points for estimating the object's position within a 3D environment. For instance, the precise localization of soccer players within a playing field has been extensively studied [34], [35], [36].

Another approach for localizing objects in 3D space is the use of distance estimations. Stereo vision is often used to estimate the distance towards an object of interest, which can be used to estimate the actual object location [37], [38].

Despite these advancements, visual tracking methods often suffer from computational complexity compared to methods involving MF or ToF sensors [39]. Techniques typically involve object detection followed by tracking algorithms or homography transformations. In contrast, MF and ToF sensors operate at higher refresh rates, potentially enhancing localization accuracy.

III. METHODOLOGY

Several strategies can be employed to estimate a vehicle's position along the driving direction within the setup

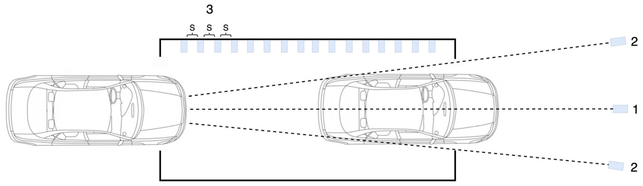

FIGURE 2. Three possible placements for ToF sensors. In the driving lane (situation 1), two sensors on the sides of the lane (situation 2), or multiple sensors on the side (situation 3).

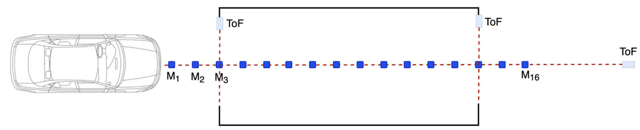

FIGURE 3. Inspection system with ToF sensor locations (red) and magnetic sensor locations (M_k). The horizontal ToF sensor measures the ground truth vehicle location.

illustrated in Figure 1. Figure 2 illustrates three potential configurations for ToF sensor placements. In situation 1, the sensor maintains an unobstructed view of the vehicle in all scenarios, but it requires positioning the ToF sensor above or below the vehicle to avoid obstructing the vehicle's path. This configuration provides consistent detection but demands careful sensor positioning.

Situation 2, eliminates the need for high or low sensor placement but requires the sensor to be positioned at a greater distance from the system and at a slight angle to achieve optimal estimation. In this situation, the vehicle is visible when entering the system, but it requires the sensor to be far away from the system to estimate the vehicle's position when exiting the system. Additionally, the performance of this setup is influenced by the shape of the vehicle's front bumper. As discussed in section II, sharp angles and rounded contours on the bumper can impair measurement accuracy with ToF sensors.

In most instances, large vehicle inspection systems impose spatial constraints when employed in operational settings. Introducing additional sensors, at extended distances outside the initial system, further limits feasible placements of the system on parking lots or other operational settings. To address this, we aim to confine sensor placement within the existing setup to reduce spatial footprint.

Situation 3 considers an alternative where multiple ToF sensors are positioned at regular intervals (s), so that cameras are triggered as each sensor detects the vehicle. While this setup allows for precise tracking, placing sensors at the system's center would interfere with the coherent light sources on the sides and roof. Alternatively, floor-mounted sensors could point upwards. However, this introduces two challenges: sensors may accumulate dirt or debris, obstructing detection, and vehicle length is restricted to the setup's dimension.

Each configuration has unique advantages and limitations, and choosing the optimal setup will depend on balancing measurement accuracy, spatial constraints, and maintenance considerations.

A. PROPOSED SOLUTION

To address the limitations identified in previous setups, we propose a multi-sensor fusion approach using Magnetic Field (MF) sensors and Time-of-Flight (ToF) sensors to estimate the vehicle location more accurately. As outlined in section II, each sensor type offers distinct advantages and limitations. By combining multiple ToF and MF sensors, we aim to enhance the accuracy and reliability of the final location estimation. The specifications of the ToF sensors and the MF sensors are specified in Appendix VI.

Our proposed system configuration, shown in Figure 3, utilizes a total of 16 MF sensors (M_k), evenly spaced at $S = 38$ centimeters. This spacing, validated experimentally, ensures sufficient overlap between the pictures to ensure that no parts of the car are left without pictures. Additionally, two ToF sensors are positioned at the entry and exit points of the inspection area. Lastly, a horizontal ToF sensor further measures the vehicle's ground truth position, solely providing a benchmark for evaluating the algorithm's performance.

The system leverages a fingerprinting method for real-time location tracking. Traditional fingerprinting methods collect data in a static offline setting for later use. However, this approach requires unique fingerprints for each vehicle model and is sensitive to environmental changes. As noted by Zafari et al. [21] and Du et al. [18], factors like nearby parked vehicles or shifts in surrounding magnetic objects may alter the fingerprint. Furthermore, variations in vehicle cargo between inspections can also affect magnetic readings, making a static fingerprint with a database impractical. Our solution needs to be adaptable across various deployment locations without requiring extensive reconfiguration or new fingerprint data collection at every location where the system will be employed.

To address these challenges, we propose an online, real-time fingerprinting approach. At the beginning of each inspection, the system dynamically generates a unique fingerprint, thereby adapting to environmental changes without requiring stored fingerprints. The ToF sensor acts as a trigger to generate the fingerprint from the MF sensors. Details of this real-time fingerprint construction process are discussed in subsection III-E.

Supporting this dynamic fingerprinting process, we introduce an algorithm featuring an interconnected state machine and tracking module. An overview of this algorithm is illustrated in Figure 4. The state machine determines if a vehicle is currently within the tracking area, using signals from the front (l_1) and rear (l_2) ToF sensors. The state machine is further detailed in subsection III-D. The tracking module, which processes inputs from the MF sensors, begins by constructing the vehicle-specific fingerprint (VS_F) when

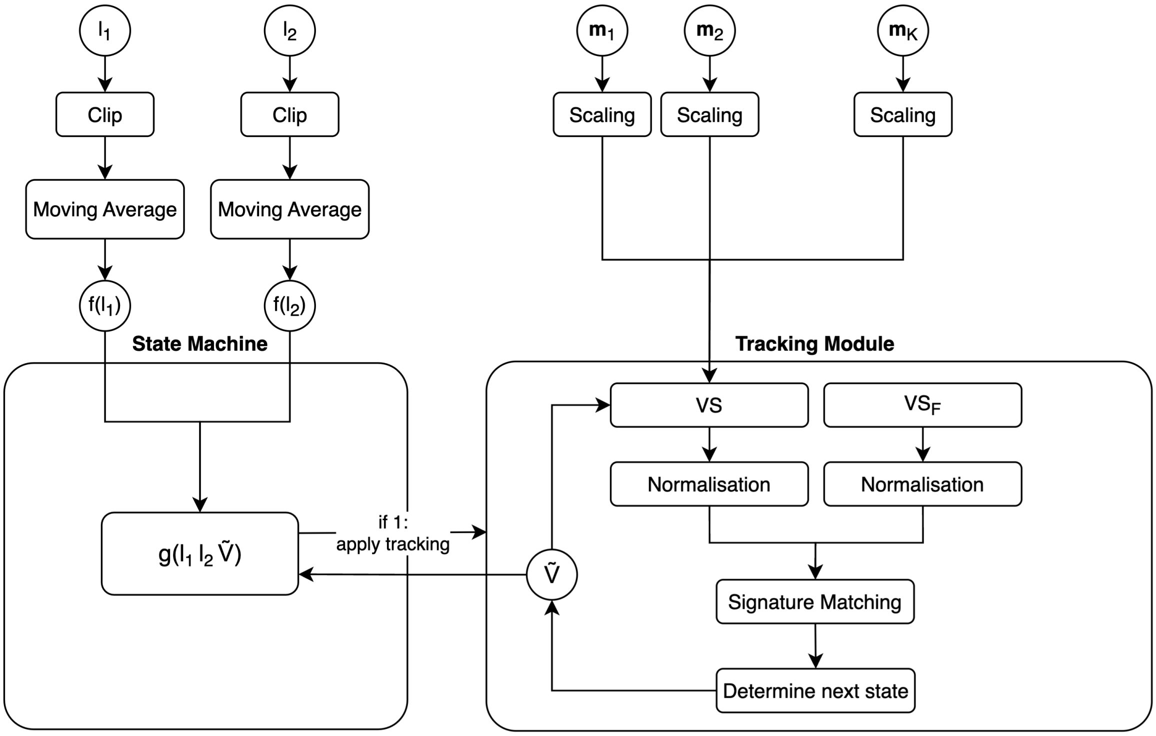

FIGURE 4. **Overview of the proposed vehicle tracking, using real-time fingerprinting.**

the inspection starts. We refer to VS_F as the Vehicle Signature, obtained from the MF sensor data, which serves as the unique vehicle fingerprint.

The algorithm's core lies in comparing this fingerprint against the real-time sensor measurements around the vehicle's current estimated position, $\tilde{v}$. By comparing VS_F to subsequent MF sensor readings, the algorithm can accurately determine movement, identifying if the vehicle is moving forward or backward. Further details on the tracking module's functionality are provided in subsection III-E.

B. DATA COLLECTION

We conducted an empirical study where data is collected from vehicles passing through the proposed setup. It is not required to stop the vehicle, which accounts for a constant flow of inspections. This is of particular importance for high-volume locations, where stopping the vehicle within the system would slow down the operational process. Therefore, we collect sensor data from the proposed setup of Figure 3, for vehicles driving through the inspection system.

To ensure diversity in our dataset, reflecting unique magnetic sensor profiles for each vehicle, we included 5 drive-through scenarios for 10 different combinations of vehicle brands and models. This approach allows us to assess the robustness of our proposed system thoroughly, as different brands and models emit different magnetic signals.

The proposed system is developed for a driving speed of 5 km/h. However, it cannot be guaranteed that drivers hold themselves to the desired driving speed. As such, we include scenario A and B to validate the proposed solution against driving with 5 km/h and with 10 km/h. When the system is employed at a high volume location, such as delivery companies, large volumes of vehicles need to be inspected at the start and end of shifts. Therefore, queues of vehicles can arise in front of the system and behind the system. Scenario C details this scenario where the speed of the vehicle is brought two times shortly to 0 km/h. This situation simulates that the vehicle has to wait twice within the system to ensure that the path out of the system is cleared from other vehicles.

Lastly, Lensor B.V. operates this inspection system with speedbumps. From this, it is known that vehicles sometimes do not have enough speed to clear the speedbump, causing them to shortly reverse during the inspection. This situation is simulated by scenario D. Scenario E simulates a vehicle reversing out of the system from the same way it entered. This situation occurs when the system is placed on a location where a drive-through is not possible. Variations in driving speed are taken into account by employing varying people for the data collection. Furthermore, changes in driving speed during the inspection is taken into account by the varying reverse or stop actions which employ changes in driving speed. We include these 5 scenarios to evaluate the robustness of the vehicle tracking system against varying types of driving behavior. The scenarios included in the collected dataset are summarized below:

A Drive-through at 10 km/h.
B Drive-through at 5 km/h.
C Scenario B and reducing vehicle speed to 0 km/h at least twice during the drive-through.
D Scenario B and briefly reversing the vehicle midway through the inspection.
E Scenario B and reverse by exiting on the same side after entering halfway.

In total, we captured 50 drive-through actions. The collected data comprises three types of variables: the ground truth distance sensor (G^t), ToF sensors (denoted as l_1^t and l_2^t), and 16 MF sensors measuring in 3 dimensions ($\boldsymbol{m}_k^t = (x_k^t, y_k^t, z_k^t)$). With this, $\boldsymbol{m}_k^t$ represents the measurement at time t for sensor k with $k \in \{0, 1, 2, \ldots, 15\}$.

The total length of the system is 600 centimeters. The MF sensors are equally spaced with spacing $s = 38$ centimeters. As such, the first sensor is placed 15 centimeters into the system. The same holds for the last sensors, being placed at 485 centimeters (600 − 15).

C. SENSOR DATA EXPLORATION

This section details the data collected from the ToF sensors and MF sensors during various vehicle inspections. Figure 5 illustrates the ground truth location for the five distinct drive-through scenarios, to visually show how the vehicle moves through the system.

The magnetic sensors measure intensity in three dimensions. Figure 6 shows the intensity for sensor 0 during inspections B and C. It is important to highlight that different brands and models exhibit different magnetic signals. As such, the sensor measurements from Figure 6 display different patterns as inspection B involves a Seat Ibiza, while inspection C involves an Audi A3. Additionally, the brief stops of the vehicle in inspection C are visible as constant sensor readings from measurements 70 to 104 and from 127 to 173.

Given the system's construction from approximately 2000 kilograms of metal, unevenly distributed, some fluctuations in sensor readings across sensors in the front or rear are expected. Furthermore, other environmental influences, such as objects placed in the near surroundings, can affect the sensor baseline. These fluctuations are depicted in Figure 7, where the baseline is different across the sensors. To account for environmental influence, the first 10 measurements of each sensor are used as an environmental benchmark. All sensor readings are adjusted accordingly, shifting them towards zero. The normalized measurements are shown in Figure 8.

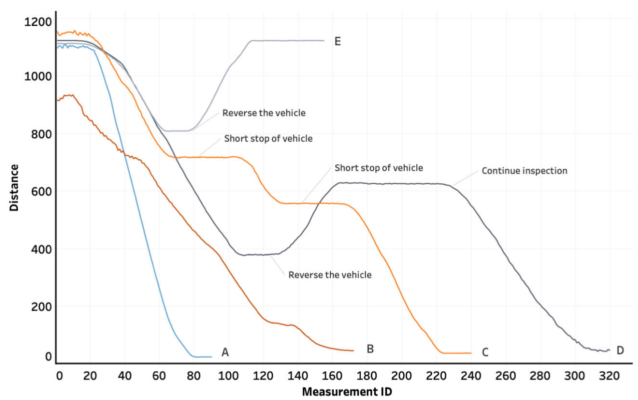

FIGURE 5. Measurements from the front reference ToF sensor, holding the ground truth location, for the 5 different scenarios.

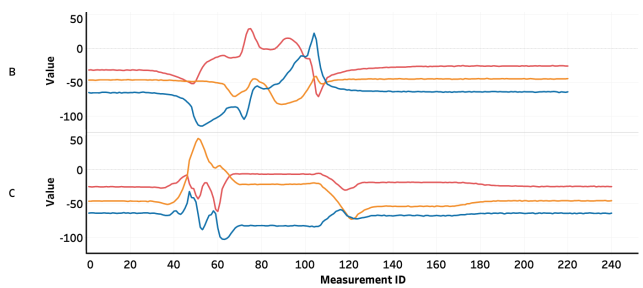

FIGURE 6. Measurements from a single sensor for all three axes during the full inspection.

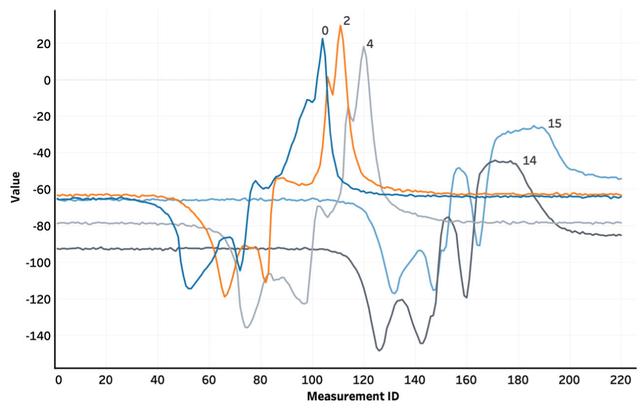

FIGURE 7. Sensor measurements for sensors 0, 2, 4, 14, and 15 for the z-axis during the full inspection.

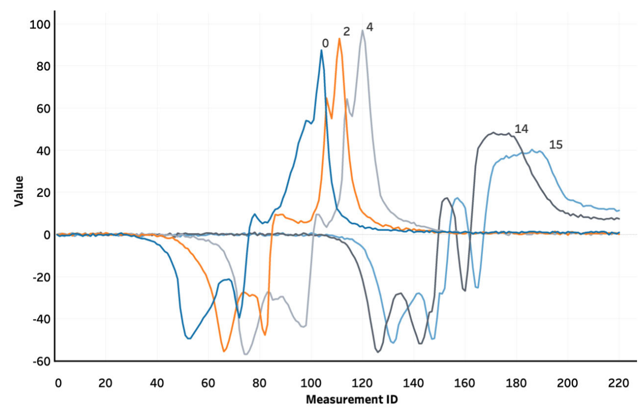

FIGURE 8. Normalized sensor measurements for sensors 0, 2, 4, 14, and 15 for the z-axis during the full inspection.

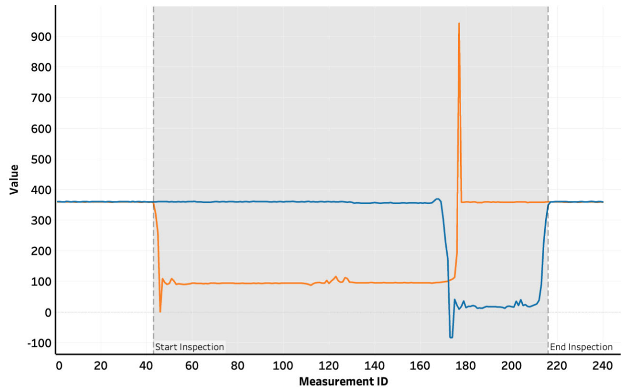

FIGURE 9. Measurements from the entry and exit ToF sensors.

From l_1 and l_2, it is determined whether a vehicle is present in the inspection area. Figure 9 shows the measurements for an inspection of scenario C. When no vehicle obstructs the sensor, the ToF sensors measure a distance of 360 centimeters. When a vehicle passes in front of the ToF sensor, the measured distance decreases depending on the vehicle's width and horizontal (y) position within the system. A significant drop below 360 centimeters indicates a vehicle is blocking the ToF sensor. Some noise is observed around measurements 46 and 177, primarily due to the curved shapes at the front and rear of the vehicle reflecting the light signal away from the sensor. This is previously pointed out as a drawback in section II.

D. STATE MACHINE

We employ a state machine to determine whether the system is idle or if an inspection is in progress. As shown in Figure 4, the state machine interacts directly with the tracking module, enabling or disabling the tracking module. The tracking module provides the vehicle's current location ($\tilde{v}$), which informs state transitions within the state machine. The five distinct states and their transitions are illustrated in Figure 10.

The system is designed to accommodate vehicles entering from both directions, ideal for deployment at parking lot

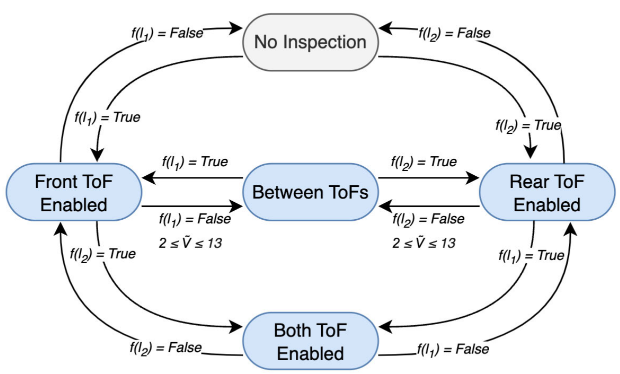

FIGURE 10. State machine, describing the five potential states and their corresponding state transitions.

entrances that function as both entry and exit points. This dual-use minimizes the number of inspection systems required while ensuring vehicles are inspected at both the start and end of a shift or rental action. As vehicles pass through, they enable either l_1 followed by l_2, or in reversed order, depending on the driving direction. If a vehicle exceeds 396 centimeters (the distance between the two ToF sensors), both ToF sensors activate simultaneously, causing the vehicle to proceed clockwise or counterclockwise along the inspection path.

Multiple preprocessing steps are applied to the raw ToF sensor data to make it robust against sensor noise and against the outliers that occur due to the round-shaped vehicles which direct the light away from the sensor, causing large spikes in the distance value as shown in Figure 9. The preprocessing steps are presented in Figure 4. In the first step, outliers are removed by clipping each measurement to the allowed ranges: $l_1 \in [0, 360]$ and $l_2 \in [0, 360]$, representing the width of the inspection system. Using a moving average, the sensor noise is further reduced. To determine if the ToF sensors are interrupted and thus activated, a binary step function is used over a moving average with $n = 2$. A relatively low $n = 2$ is empirically obtained from the dataset, where $n = 1$ resulted in 12 false alarms on the full dataset. $n = 2$ is the minimal value of n without any false alarms. A higher value of n will further reduce the probability of a false alarm. However, it will also delay the detection, causing the inspection to potentially start too late. The ToF sensor activation for sensor i at time t is defined by $f_t(l_i^t)$ in Equation (1).

$$f_t(l_i^t) = \begin{cases} 1 & 50 \leq \frac{1}{n} \sum_{j=t-n}^{t} l_i^j \leq 150, \\ 0 & else. \end{cases} \tag{1}$$

For vehicles longer than 396 centimeters, the activation function ($g_t(l_1^t, l_2^t)$), indicating whether a vehicle is within the system, is expressed by Equation (2). For vehicles shorter than 396 centimeters, the first ToF sensor will be disabled before the second ToF sensor is activated. Figure 10 presents this state in the center of the state machine. To overcome this, we incorporate the output of the Tracking Module ($\tilde{v}$). The tracking module is further detailed in subsection III-E. We extend $g_t(l_1^t, l_2^t)$ by incorporating vehicle location estimate $\tilde{v}$ and state that there is no vehicle if both ToF sensors are disabled and the sensors tracking does not indicate a vehicle in the range [2, 13]. With this, the tracking module improves the state machine by drawing a connection between the MF sensors and the ToF sensors. The resulting $g_t(l_1^t, l_2^t, \tilde{v})$ is presented in Equation (3). The resulting values from $f_t(l_i^t)$ and $g_t(l_1^t, l_2^t, \tilde{v})$ are presented in Figure 11. We omit t in the equations for readability.

$$g(l_1, l_2) = \begin{cases} 1 & \max_{i \in \{1,2\}} f(l_i) = 1, \\ 0 & else. \end{cases} \tag{2}$$

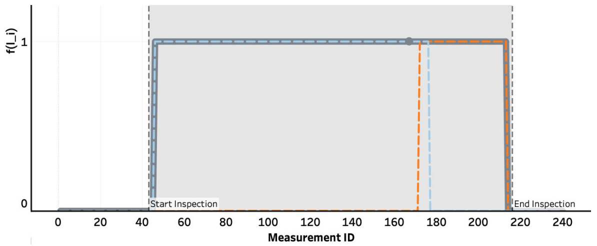

FIGURE 11. Resulting ToF activation ($f(l_1)$ and $f(l_2)$) in dashed lines and the thick grey line representing a vehicle in the inspection system ($g(l_1, l_2, \tilde{v})$).

$$g(l_1, l_2, \tilde{v}) = \begin{cases} 1 & \max_{i \in \{1,2\}} f(l_i) = 1 \ or \ 2 \leq \tilde{v} \leq 13, \\ 0 & else. \end{cases} \tag{3}$$

E. TRACKING MODULE

We propose integrating a tracking module in conjunction with the previously defined state machine (subsection III-D). The tracking module is designed to determine, at any given time t, whether the vehicle has moved forward to the next sensor ($\tilde{v} + 1$), remained at its current sensor ($\tilde{v}$), or moved backward to the previous sensor ($\tilde{v} - 1$). This allows the module to determine whether the vehicle has remained in place or shifted by $S = 38$ centimeters in either direction.

The tracking module is activated when the state machine transitions from the *No Inspection* state to either the *Front ToF Enabled* or *Rear ToF Enabled* states, i.e., when $g(l_1, l_2, \tilde{v}) = 1$. Figure 12 illustrates a schematic of a vehicle, shorter than 396 centimeters, passing through the tracking system. This schematic presents how the vehicle moves past the ToF sensors and the MF sensors while driving through the system. Figure 8 demonstrates a consistent pattern in the data from each sensor, where the signal from each subsequent sensor ($k + 1$) lags behind the previous one (k) by t time steps. This lag represents the time taken for the vehicle to travel between consecutive sensors, with longer lags corresponding to slower speeds.

To detect these patterns, we propose employing time-series matching with a fingerprinting technique. This approach aims to identify when the signal observed at sensor k reappears at sensor $k + 1$, thereby enabling precise tracking of the vehicle's movement across sensors. The subsequent subsections of Figure 12 present the start of the tracking with the real-time fingerprint construction (1), the matching (2 and 4), the proposed reverse tracking (3), and the end of the inspection (5).

1) FINGERPRINT CONSTRUCTION

Figure 12 (1) marks the activation of the tracking module. The ToF sensors and MF sensors work together to generate the Vehicle Signature (VS) which is used as the fingerprint. The process begins when the front of the vehicle interrupts the first ToF sensor, triggering the construction of the VS_F. This signature incorporates the previous p measurements from the MF sensors, where p represents the length of the VS. The graphical representation of Figure 12 illustrates a fingerprint being derived from the three green MF sensors on and before the ToF sensor.

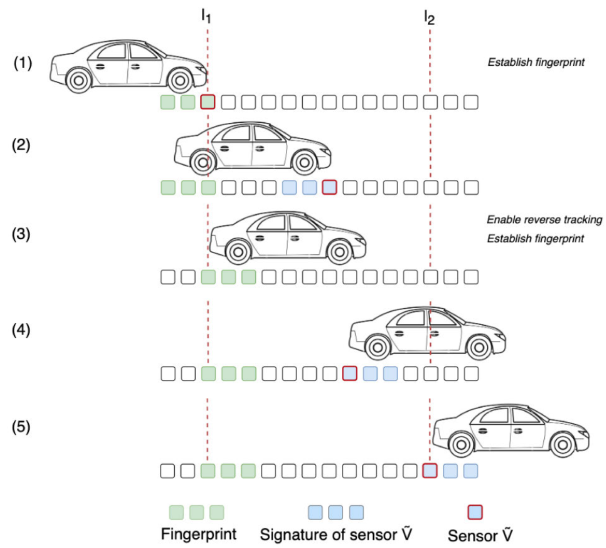

FIGURE 12. Schematics of the ToF sensor placement and the MF sensor placement with respect to the vehicle. The different stages of the proposed tracking algorithm are presented with the sensors for the fingerprint, signature of sensors $\tilde{v}$, and the ToF sensors.

Figure 8 reveals that the sensors are not perfectly uniform, with some noise observed in the data. In addition, multiple sensors can simultaneously interact with the vehicle due to the small distance between each sensor. To address this, we propose a VS design that spans the temporal dimension, multiple sensors, and the three dimensions of the MF sensor.

The final vehicle signature is depicted in Figure 13 as a 3D matrix of dimensions $p \times r \times 3$, where p is the signature length, r is the number of sensors included in the pattern, and 3 represents the dimensions of the MF sensors. Extending the pattern across a longer history, multiple sensors, and their respective dimensions can improve the stability of vehicle tracking.

This real-time collaboration between the ToF and MF sensors enables dynamic construction of the vehicle signature, eliminating the need to pre-store signatures for specific vehicle brands or models, as commonly required in previous research. Furthermore, this approach ensures that tracking remains unaffected by changes in the vehicle's cargo, which could otherwise alter its fingerprint.

2) REVERSE TRACKING

The vehicle's front is typically used to construct the fingerprint. However, as the vehicle exits the system (Figure 12 (4)), front sensors can no longer detect the vehicle, while the rear remains within the system and requires tracking to determine

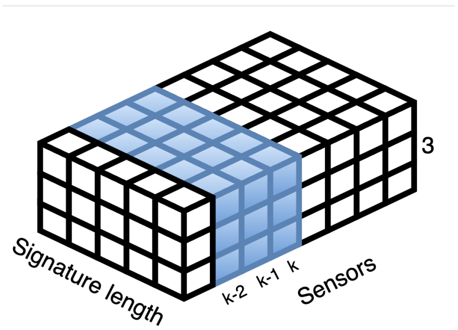

FIGURE 13. Matrix representation of the Vehicle Signature for signature length *p*, *r* sensors, and 3 MF sensor dimensions.

if a camera capture is necessary. To avoid placing additional sensors outside the system, we switch the tracking focus from the front to the rear of the vehicle during the inspection.

Figure 12 illustrates the proposed reverse tracking method. Initially, the fingerprint is constructed based on the front of the vehicle when it interrupts the first ToF sensor (position 1). Upon reaching position (3), the front ToF sensor is no longer interrupted, and a new fingerprint is generated using the rear of the vehicle. From this point onward, the rear fingerprint is used to track the vehicle until it fully exits the system (position 5).

For optimal signal strength, sensors located beneath the vehicle are used to construct the fingerprint. During front tracking (positions 1 and 2), MF sensors positioned before the ToF sensor are utilized. In rear tracking (positions 3, 4, and 5), MF sensors located after the ToF sensor are employed. The sensors contributing to the fingerprint are highlighted in green for clarity.

3) VEHICLE SIGNATURE MATCHING

Figure 14 provides a graphical overview of the proposed tracking and matching algorithm. The algorithm begins with the vehicle's current position ($\tilde{v}$) as input. The possible states ($\tilde{v} + z$) are defined as the allowed vehicle movements relative to sensor $\tilde{v}$, where $z \in Z$ and $Z := \{-z_b, \ldots, 0, \ldots, z_f\}$. Here, z_b represents the maximum number of steps backward, and z_f represents the maximum number of steps forward. For illustration, Figure 14 visualizes the algorithm under the conditions $z_b = 1$ and $z_f = 1$.

To determine whether the vehicle moves out of its current position, the algorithm performs a time-series comparison between the fingerprint ($\boldsymbol{VS_F}$) and the signatures of the candidate states ($\boldsymbol{VS_{k+z}}$). Notably, the fingerprint is not updated at every time step. Instead, it is established and locked at specific positions, such as positions (1) and (3) in Figure 12. The similarity between $\boldsymbol{VS_F}$ and $\boldsymbol{VS_{k+z}}$ is defined by:

$$sim\big(\boldsymbol{VS_F}, \boldsymbol{VS_{k\mathcal{C}z}}\big); \forall z \in Z. \tag{4}$$

To illustrate the evaluated comparisons, we highlight situation (2) of Figure 12. The vehicle signature is constructed when l_1 is interrupted at time $\tilde{t}$, making $\boldsymbol{VS_F}$ equivalent to $\boldsymbol{VS_2}$ of $\tilde{t}$. The comparison at time t is made between $\boldsymbol{VS_F}$ and moving backward $\boldsymbol{VS_7}$, staying in the current state $\boldsymbol{VS_8}$, or moving forward $\boldsymbol{VS_9}$.

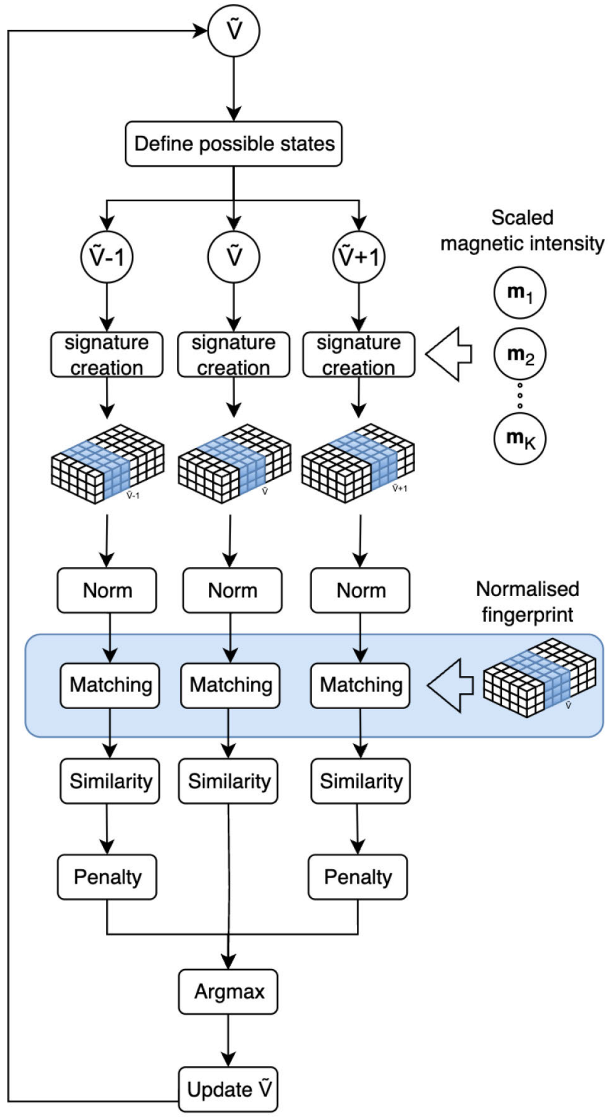

FIGURE 14. Overview of the vehicle matching algorithm.

Various similarity functions are available to evaluate this matching. We approach the task as a time-series similarity problem, commonly implemented using the Minkowski distance [40], [41], [42]. However, vehicle motion introduces non-stationary variances, and sensor amplitudes can vary significantly, as highlighted in Figure 8. To address this, alternative measures like the Mahalanobis distance, which accounts for non-stationary variances, may improve matching accuracy [43], [44].

To mitigate amplitude differences, Chen et al. [45] proposed a correlation matrix combined with the Pearson correlation coefficient, while Nakamura et al. [46] utilized cosine similarity, which is less sensitive to outliers than standard correlation methods. Equation (5) demonstrates the application of cosine similarity for VS matching.

$$sim(VS_k, VS_{k\mathcal{C}_z}) = \frac{\langle \mathbf{VS_k}, \mathbf{VS_{k+z}} \rangle}{\|VS_k\| \, \|VS_{k\mathcal{C}_z}\|}. \tag{5}$$

Alternatively, we recommend normalizing signatures using the Euclidean Norm ($L2$). This approach emphasizes the shape of the signature over its amplitude, potentially enhancing robustness to environmental and sensor noise. From this, Minkowski distances can be used to compare the signatures. We employ this combination in the normalization step of Figure 14.

As it can be expected that not every sensor and every sensor dimension within the VS will be equally important, we weigh the measurements from the sensor by the sensor dimension importance α. Similarly, we apply a weighted average across sensors in the signature (r) to account for varying sensor importance. The weights for sensors are represented by the sensor importance vector, β.

The final matching function, presented in Equation (6), computes the weighted similarity by integrating both sensor and dimension importance, outputting a comprehensive similarity score over all sensors (r) and their three dimensions. Equation (6) presents the matching using the MAE. In our research, we evaluate the performance of the cosine similarity for the signature matching and compare this performance with applying the Euclidean Norm normalization in combination with the MAE.

$$sim(VS_F, VS_{k\mathcal{C}_z}) = \sum_{i=1}^{r} \beta_i \sum_{j=1}^{3} \alpha_j \frac{1}{p} \sum_{t=1}^{p} \left| VS_F^{t,i,j} - VS_{k+z}^{t,i,j} \right| \tag{6}$$

4) PENALTY FUNCTION

Based on practical observations, it is assumed that vehicles typically move either one step forward or backward per time unit, with a smaller likelihood of moving two steps. Additionally, vehicles are more inclined to progress forward through the inspection area than to reverse during the inspection.

To minimize unnecessary oscillation between sensors, we aim to prevent forward and backward jumps when the difference in similarity is negligible. Such situations often occur when a vehicle is positioned (stationary) between two sensors.

As such, we introduce two penalty functions. The first penalty function penalizes a movement from sensor k to any sensor $k + z$ where z is positive. The second empowers a penalty when z is negative. In addition, we increase the penalty with a magnitude of the number of moved steps, resulting in the following penalty function:

$$g(k, z) = \begin{cases} z \cdot p_b & z < 0, \\ 0 & z = 0, \\ z \cdot p_f & z > 0. \end{cases} \tag{7}$$

5) DYNAMIC VEHICLE SIGNATURE (DVS)

Variations in sensor patterns at different locations within the system are detailed in subsection III-C and illustrated in Figure 8. When using the proposed methodology, high similarity is observed between adjacent sensors, while sensors located farther apart within the system exhibit lower similarity by default. Based on this observation, we recommend adopting a Dynamic Vehicle Signature (DVS) instead of a Fixed Vehicle Signature (FVS).

In the previously described Fixed Vehicle Signature (FVS), the fingerprint is updated only at the start of the inspection (Figure 12 (1)) and at the beginning of reverse tracking (Figure 12 (3)). By contrast, the DVS dynamically adjusts the fingerprint, updating the signature whenever the vehicle transitions to a new sensor location. The initial pattern is created similarly to the process outlined in Figure 12 (1). Subsequently, each sensor change prompts the generation of a new fingerprint.

The primary advantage of the DVS is its ability to adapt dynamically to environmental changes, accounting for both internal system variations and external factors such as nearby vehicles or metallic objects in the vicinity of the system.

6) DYNAMIC VEHICLE SIGNATURE LENGTH (DVS-L)

Determining an appropriate value for the Vehicle Signature length (p) is challenging due to significant variations in driving speed during inspections. The number of measurements captured between sensor movements fluctuates with the vehicle speed. Higher speeds yield fewer measurements per sensor movement.

The optimal value of p can also depend on changes in vehicle speed during inspection or brief stops. A smaller p enables the pattern to adapt quickly to changes, while a larger p adapts more gradually but provides greater tracking stability.

To address this, we propose using a Dynamic Vehicle Signature Length (DVS-L). Initially, a default p value is selected, with subsequent adjustments determined by the number of measurements recorded between each sensor movement. More formally, p is defined by the number of measurements ($\boldsymbol{m_k}$) recorded between sensor k and sensor $k - 1$. To avoid large fluctuations, we constrain p within the range $p \in [2, 2\tilde{p}]$, where $\tilde{p}$ is the initial value of p. This approach is summarized in Equation (8), which defines the value of p at sensor k.

$$p(m_k) = \begin{cases} 2 & m_k < 2, \\ p & 2 \le m_k \le 2\tilde{p}, \\ 2\tilde{p} & m_k > 2\tilde{p}. \end{cases} \tag{8}$$

7) SUPPORTING ARBITRARY VEHICLE LENGTH

Our proposed solution indicates the start and end of the vehicle within the system, precisely identifying the area occupied by the vehicle. This allows for the precise triggering of each camera based on the vehicle's exact location. However, tracking only the front or rear of the vehicle imposes a limit on the maximum vehicle length that can be tracked within the system, which is 496 centimeters (600 − 104 centimeters). To accommodate vehicles exceeding this length or to support smaller hardware setups, a slight modification can be implemented.

In this approach, we avoid continuously moving the pattern across the sensors. The vehicle signature is established when the vehicle first activates the ToF sensor. As the vehicle signature aligns with the next MF sensor, it indicates that the vehicle has moved past one sensor. Similar to the previous implementation, a vehicle signature is generated; however, now an additional signature is created from the same MF sensor aligned with the ToF sensor. This process continues until either the front of the vehicle reaches the second ToF sensor or the rear reaches the first ToF sensor. At this point, the ground truth pattern shifts to the relevant sensor. This method allows the system to track vehicles of any length while accurately maintaining information about the vehicle's front and rear positions.

We compare the results of this tracking solution against the earlier proposed solution in section IV.

F. EVALUATION FUNCTION

To evaluate the robustness of the tracking algorithm, we compare the ground truth location (d_t) against the predicted location ($\hat{d}_t$) using the Mean Absolute Error (MAE) as presented in Equation (9). We omit the usage of a scaled error metric as the system is a closed environment with an equal amount of MF sensors in every data sample.

$$MAE = \frac{1}{T}\sum_{t=1}^{T} |d_t - \hat{d}_t|. \tag{9}$$

G. PARAMETER TUNING

The effectiveness of the proposed vehicle tracking algorithm relies heavily on the choice of parameters. Increasing the pattern length enhances tracking stability but results in slower adaptation to changes in vehicle speed. Similarly, parameters like the penalty function and the weight assigned to magnetic dimensions significantly influence tracking performance.

To optimize the parameters, we employ a grid search method, dividing the dataset into a train set and a test set. The entire dataset, detailed in subsection III-B, comprises 10 vehicles across 5 distinct drive-through scenarios. Consequently, we partition the dataset with 7 vehicles (35 drive-through actions) allocated for testing, and the remaining 3 vehicles (15 drive-through actions) designated for tuning the parameters.

The parameter ranges for the search are listed below. For this, we define the set $S_{0.2}$ as $\{x \in \mathbb{R} \mid x = 0.2 \cdot k,\ k \in \mathbb{Z},\ 0 \le k \le 5\}$.

$$\begin{cases} p & \in \{x \in \mathbb{Z} \mid 1 \le x \le 15\} \\ r_1 & \in S_{0.2} \\ r_2 & \in S_{0.2} \\ r_3 & \in S_{0.2} \\ \text{DVS} & \in \{\mathit{True}, \mathit{False}\} \\ \text{DVS-L} & \in \{\mathit{True}, \mathit{False}\} \\ \tilde{m}_x^t & \in S_{0.2} \\ \tilde{m}_y^t & \in S_{0.2} \\ \tilde{m}_z^t & \in S_{0.2} \\ p_f & \in S_{0.2} \\ p_b & \in S_{0.2} \end{cases} \tag{10}$$

IV. RESULTS

Applying the parameter tuning of subsection III-G, an MAE of 0.3115 is achieved across all samples in the test set. The best-performing sample achieves an MAE of 0.0942 and the worst-performing sample results in an MAE of 0.7631. The optimized parameters are listed in Equation (11). Interestingly, the best settings are found without the DVS and without the DVS-L. DVS enabled (True) results in a 32% higher MAE, compared to DVS disabled (False). Furthermore, the Euclidean norm normalization with the MAE outperforms the Cosine similarity by over 14%. As such, all following results are presented for the Euclidean norm normalization with the MAE.

$$\begin{cases} p & := 5, \\ r_1 & := 1.0, \\ r_2 & := 1.0, \\ r_3 & := 1.0, \\ \text{DVS} & := \mathit{False}, \\ \text{DVS-L} & := \mathit{False}, \\ \tilde{m}_x^t & := 0.6, \\ \tilde{m}_y^t & := 1.0, \\ \tilde{m}_z^t & := 1.0, \\ p_f & := 0.2, \\ p_b & := 0.2. \end{cases} \tag{11}$$

The algorithm performance with the optimized parameters is evaluated on the test set. Figure 15 presents the MAE box plot for each of the five driving scenarios (Figure 5). Every box plot holds the seven samples from the test set. Scenario C shows large extremes in the MAE over the different samples, where the results for Scenario A and B are more centered around the median. Scenarios C, D, and E hold more changes in driving speed, including complete stops of the vehicle (stationary). This seems to result in larger interquartile ranges, with more variation in the algorithms' performance on different samples.

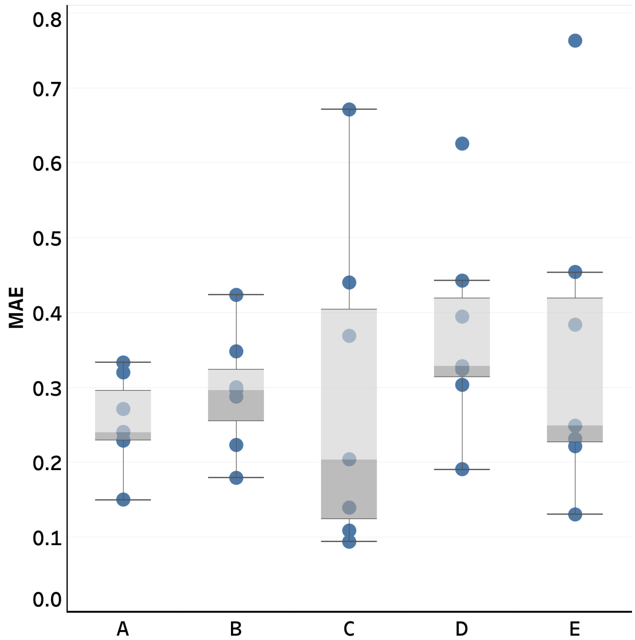

FIGURE 15. MAE on the test set, separated over the five different driving scenarios.

TABLE 1. MAE, relative error concerning 16, 32, and 64 sensors, and the error in centimeters for the varying number of sensors.

# Sensors	MAE	Relative MAE	Error in centimeters
16	0.3115	100.0%	11.84
32	0.3153	101.21%	5.99
64	0.3191	102.45%	3.03

In Figure 16, we present varying samples from the tracking algorithm. It shows the ability of the proposed algorithm to adapt to speed changes (scenarios C, D, and E) and when reversing the vehicle within the system (scenarios C and D). Furthermore, the algorithm quickly adapts when the vehicle starts driving after standing still, largely due to the low value of $p = 5$.

Figure 17 presents the captured images from 2 different vehicle inspections for 2 different camera angles, using the same vehicle. It shows the extreme relevance of the tracking system, as cameras with a straight angle on the vehicle require more captures compared to cameras under an angle. Therefore, the capture frequency can be set differently per camera, using the tracking algorithm. Furthermore, the images across the two inspections show that the tracking algorithm is able to create consistency and capture the same area of the vehicle per image. With this, we show how the results from Figure 16 are translating to better quality vehicle inspections.

A. PARAMETER INFLUENCE

1) TRACKING GRANULARITY

We evaluate if the tracking performance gets influenced when the number of sensors in the tracking algorithm increases. The benefit of additional sensors is the increased granularity, where the vehicle can be tracked in smaller steps of sensor distance S. Table 1 presents the relative MAE for the proposed algorithm on respectively 16, 32, and 64 sensors. The results show that the tracking performance is only marginally influenced when doubling or quadrupling the number of sensors. However, the tracking performance in centimeters gets improved drastically due to the reduced sensor distance when more sensors are applied.

2) PENALTY FUNCTION

Figure 18 presents the influence of the penalty function on the MAE. It shows the algorithm's relative performance concerning the optimized settings from the parameter tuning. It can be seen that increasing the penalty function in either of the two dimensions largely impacts the MAE negatively. Despite this, introducing the penalty function to the algorithm ($p_f = 0.2, p_b = 0.2$) does reduce the MAE with approximately 4%.

3) SIGNATURE LENGTH

Figure 19 shows the impact of the signature length on the MAE. The graph presents the best-found MAE for the provided signature length and is split out over the different scenarios. It shows that scenarios D, and E suffer stronger from a larger signature length. Both scenarios include reversing the vehicle which could explain the negative impact of longer signatures. Scenario C does not seem to be impacted to a large extent when the signature length is changed. Selecting the smallest possible signature length is of importance to reduce computational requirements from the algorithm.

B. ARBITRARY VEHICLE LENGTH

To evaluate if the support of arbitrary vehicle length impacts the tracking performance, we compare the average tracking error in Table 2. It shows the average error across all samples, as well as the error per scenario, to explore if one of the two approaches is superior for specific types of driving behavior. It shows the relative performance of the arbitrary vehicle length approach, with respect to the original implementation. Solely, scenario C and D show a significant difference, where scenario C results in a 2.12% higher error and scenario D in a 2.47% lower error.

TABLE 2. Error of the arbitrary vehicle length approach, concerning the original tracking method. Bold percentages present significant changes under $p = 0.05$.

Scenario	Relative Error
A	100.23%
B	100.10%
C	**102.12%**
D	**97.53%**
E	99.80%
Average	99.93%

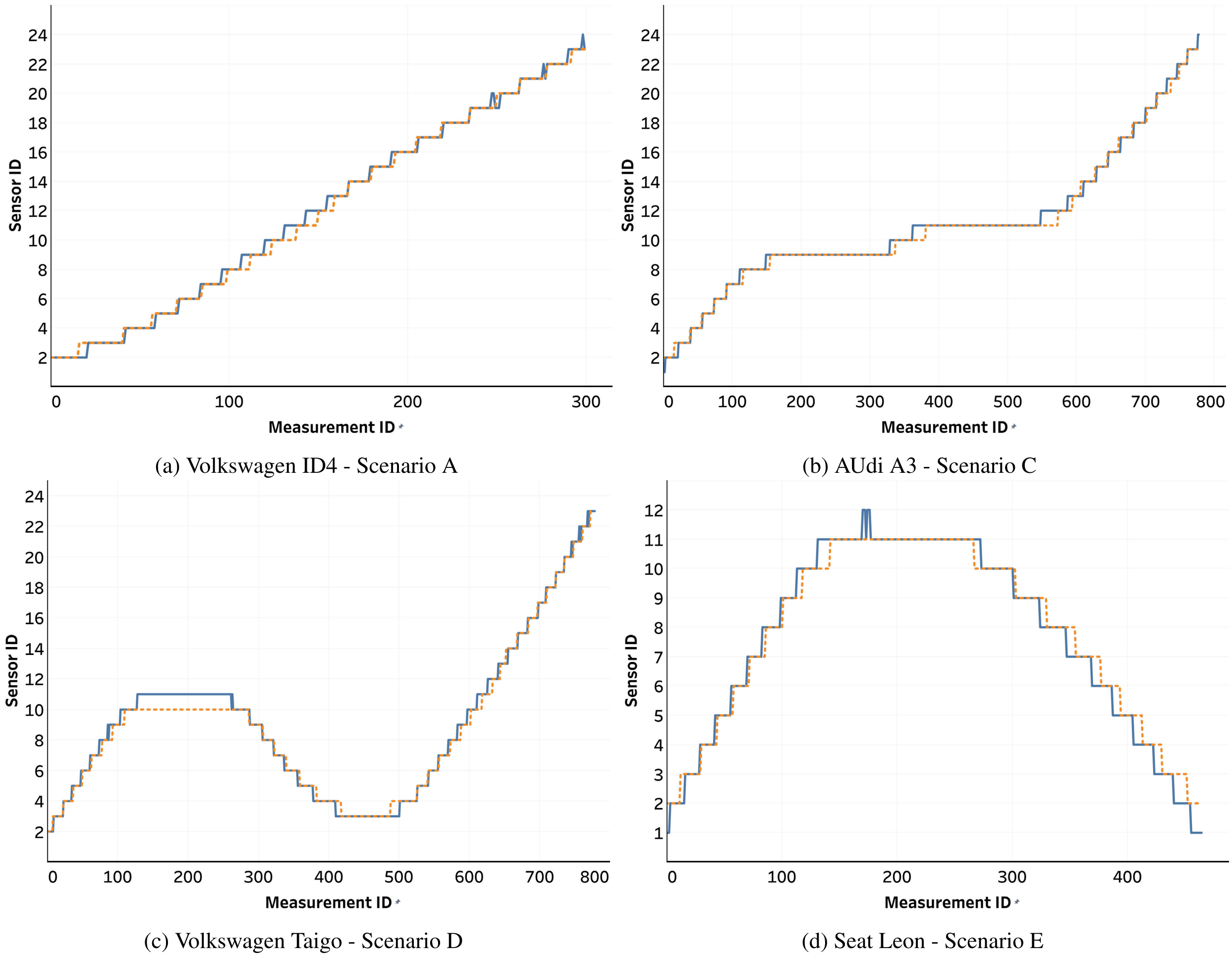

(a) Volkswagen ID4 - Scenario A

(b) AUdi A3 - Scenario C

(c) Volkswagen Taigo - Scenario D

(d) Seat Leon - Scenario E

FIGURE 16. Excerpt from the test set. The solid blue line indicates the ground truth, whereas the dashed orange line indicates the prediction. We omit an excerpt from scenario B as it is relatively comparable with scenario A.

FIGURE 17. 2 inspections under 2 different camera angles. The first inspection is presented on row 1 and 3 and the second inspection on row 2 and 4.

C. DATA VOLUME REDUCTION

Data from the MF sensors is collected at a rate of 70 Hz. With this polling rate, a total of 1120 measurements are collected from the MF sensors every second. We present the tracking error (MAE) in Figure 20, as a function of the MF sensor polling rate in (Hz) on the x-axis.

P_b \ P_f	0	0,2	0,4	0,6	0,8	1
0	104%	103%	107%	115%	119%	123%
0,2	101%	100%	109%	117%	119%	126%
0,4	112%	110%	111%	119%	123%	130%
0,6	119%	115%	119%	122%	127%	141%
0,8	124%	121%	131%	139%	139%	142%
1	131%	137%	140%	141%	145%	148%

FIGURE 18. Relative influence of the penalty function (P_f and P_b), concerning the optimized settings of $P_f = 0.2$ and $P_b = 0.2$.

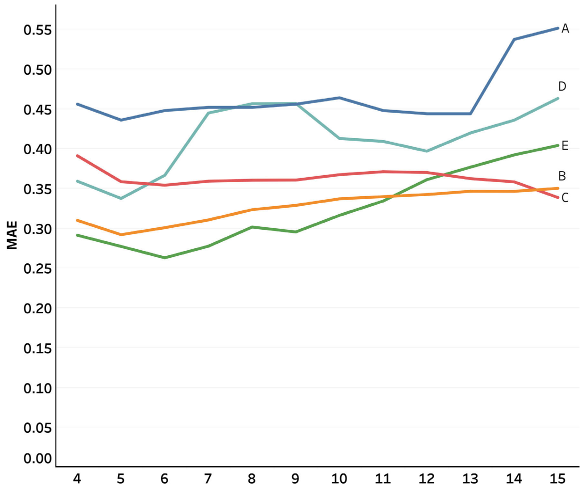

FIGURE 19. Influence of the signature length on the MAE. The graph presents the best-found MAE for the given signature length. Results are separated on the DVS.

The graph shows a clear relationship between the MAE and the polling rate in Hz. However, there is a diminishing return when the polling frequency is increased. In that way, halving the 70 Hz to 35 Hz adds 12.5% to the error. Therefore, if less accuracy is accepted, the polling rate can be reduced to reduce the processing requirements. On the other hand, it indicates that increasing the polling rate above the 70 Hz will most likely result in limited benefits.

D. TIME COMPLEXITY

1) THEORETICAL TIME COMPLEXITY

The proposed algorithm's time complexity is analyzed per timestep. Preprocessing involves thresholding ToF lidar data over n historical readings for 2 sensors ($O(n)$) and applying an activation function ($O(1)$). The core matching compares the fingerprint ($p \times r \times 3$) with those of neighboring vehicle states ($v - 1$ and $v + 1$). This involves normalizing the fingerprint vectors with the Euclidean norm normalization ($O(p \cdot r)$) and computing their similarity using a summation over p timesteps, r sensors, and 3 dimensions as presented in Equation (6) ($O(p \cdot r)$). A constant-time penalty function is then applied.

Considering the dominant operations, the normalization and similarity computation steps, each performed twice (for preceding and succeeding states), dictate the overall complexity. Therefore, the time complexity of the fingerprint matching algorithm for each timestep is $O(p \cdot r)$, indicating a linear scaling with the number of considered past timesteps (p) and the number of sensors (r). The preprocessing step's complexity of $O(n)$ is a lower-order term in the overall per-timestep analysis.

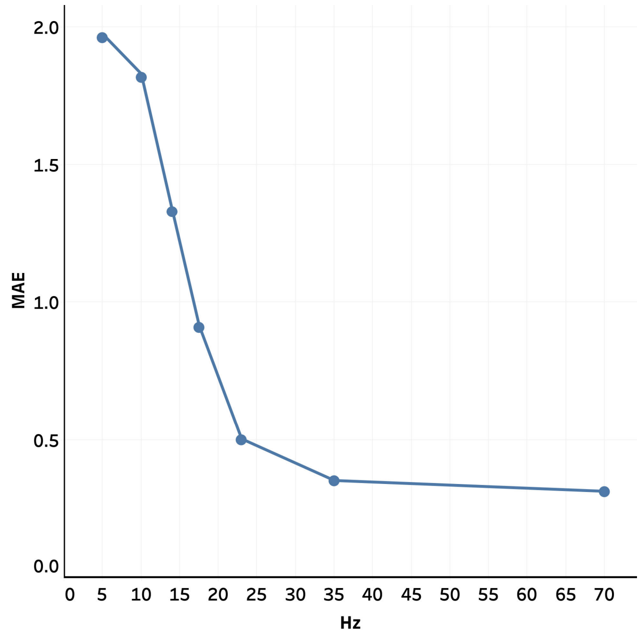

FIGURE 20. The tracking error (MAE) as a function of the MF sensor polling rate in (Hz).

TABLE 3. Average time per iteration through the full algorithm (preprocessing, state machine, and matching) with 2 Time-of-Flight (ToF) sensors and 32 Magnetic Field (MF) sensors. The comparison is limited to CPU processing only.

System	Average Iteration Time (ms)	Average Iteration rate (Hz)
Raspberry Pi 5 8GB	0.272	3676
Jetson Nano 4GB	0.181	5524
Apple Silicon M2 Pro 32GB	0.084	11904

2) EVALUATION ON DIFFERENT DEVICES

In addition to the theoretical time complexity, we evaluate the algorithm in practice on varying systems. Table 3 presents the number of algorithm updates that can be processed on average per device. In other words, the maximum Hz can be processed from the algorithm side with 2 ToF sensors and 32 MF sensors. The comparison is drawn for CPU processing only to show the potential update rate of the proposed algorithm.

V. DISCUSSION

The proposed implementation makes use of 16 MF sensors and 2 ToF sensors. Therefore, effective calibration and precise parameter tuning are crucial. We have extensively tested the system's robustness across various vehicle brands, models, and driving behaviors. Despite this, we suggest further research to collect a larger dataset to validate the robustness of the algorithm against a larger set of vehicle brands and models.

While adjustments have been made to compensate for background noise, robustness tests concerning disturbances in the magnetic field during the inspections have not been fully incorporated. Further research could investigate the algorithm's resilience to such changes. We suggest extending the dataset with samples where magnetic objects move closely around the tracking system, while the tracking is employed. This can highlight additional requirements regarding background noise compensation and might result in changes in the normalization of the algorithm.

Currently, the MF sensors are spaced 38 centimeters apart, when 16 sensors are employed. Evaluations with 32 and 64 sensors showed the tracking capabilities for a larger number of sensors with a smaller sensor distance. However, the tracking remains a discrete match. Therefore, we suggest further research to extend our proposed algorithm to a continuous implementation. Having the ability to estimate the vehicle position when it is positioned between two sensors can increase its granularity and reduce the overall complexity of the hardware setup. A continuous approach will remove the need to scale the number of sensors when a higher tracking granularity is required.

The proposed algorithm is currently not focused on tracking multiple vehicles simultaneously, as the proposed vehicle inspection system fits solely one vehicle. However, there might be situations, such as assembly lines, where tracking multiple vehicles might be of relevance. As such, we suggest further research to extend this algorithm to accommodate tracking of multiple vehicles simultaneously. For this, we suggest further research to extend the state machine to accommodate multiple vehicles and multiple vehicle locations v in the system.

VI. CONCLUSION

We propose an advanced system that integrates Magnetic Field sensors and Time-of-Flight sensors with a sophisticated vehicle tracking algorithm to monitor precise vehicle movement within an inspection system.

Diverging from previous approaches, our proposed solution eliminates the need for offline data collection, prior knowledge of the vehicle, or sensors attached to the vehicle. Instead, we propose sensor fusion to establish a real-time fingerprint. This fingerprint is created when the vehicle enters the system, avoiding the need to store a fingerprint for every vehicle brand, model, and year combination. Furthermore, it removes the need to calibrate the system in different environments and makes it robust to payload changes that can affect the tracking when collected in an offline environment.

We compiled a dataset featuring 10 distinct vehicles from various makes and models, subjected to testing across 5 different driving scenarios, totaling 50 inspections. Using this dataset for meticulous parameter optimization, our system achieves vehicle tracking with an average error of 0.3115 sensor lengths across all samples. We present the robustness of the proposed algorithm against different real-world driving scenarios. The findings highlight the algorithm's exceptional performance, particularly in scenarios involving complete stops of the vehicle during the drive-through process, or when vehicles change driving direction multiple times during the inspection.

However, the inter-quartile range of the MAE is lower for inspections with constant driving speed than when the vehicle changes driving speed, stops during the inspection, or changes driving direction.

Furthermore, we show that the proposed algorithm can scale to more sensors without compromising the sensor-matching performance. We evaluate the MAE when double or quadruple the number of sensors, which shows that the MAE increases respectively 1% and 2%. With this, we present that by doubling or quadrupling the number of sensors, the absolute error is reduced from 11.84 centimeters to respectively 5.99 centimeters and 3.03 centimeters. This shows the scalability of the algorithm towards more sensors and more granularity in the tracking.

While our parameters were fine-tuned based on this specific vehicle dataset, we are confident in the system's potential to generalize for tracking other magnetic objects.

APPENDIX A
SENSOR SPECIFICATIONS

See Tables 4 and 5.

TABLE 4. Specifications of the MF sensors (Bosch BMM350) [47].

Parameter	Value
Sensor type	3-axis TMR magnetometer
Measurement range	$\pm 2000\,\mu$T (X, Y, Z axes)
Resolution	$0.10\,\mu$T
Accuracy	$\pm 25\,\mu$T zero-field offset
Sample rate	up to 400 Hz
Supply voltage	3.3–5.0 V
Power consumption	$200\,\mu$A @ 100 Hz
Operating temperature	$-40°$C to $85°$C
Communication interface	I2C, I3C
Enclosure	$1.28 \times 1.28 \times 0.50$ mm

TABLE 5. Specifications of the ToF sensors (Benewake TFmini Plus LiDAR) [48].

Parameter	Value
Sensor type	ToF LiDAR
Field of view (FOV)	3.6°
Measurement range	0.10–12.00 m
Resolution	5.0 mm
Accuracy	± 5.0 cm (0.10–6.00 m), $\pm 1\%$ (6.00–12.00 m)
Sample rate	1–1000 Hz (adjustable)
Supply voltage	$5.0\,\text{V} \pm 0.5\,\text{V}$
Power consumption	550 mW (average), 85 mW (low power)
Operating temperature	$-20°$C to $60°$C
Wavelength	850 nm (LED)
Communication interface	UART, I2C
Enclosure	$35.0 \times 21.0 \times 18.5$ mm

ACKNOWLEDGMENT

The authors would like to thank Lensor for contributing to this research by providing a test location, hardware, and test vehicles.

REFERENCES

[1] H. Wang, Z. Xiong, A. M. Finn, and Z. Chaudhry, "A context-driven approach to image-based crack detection," *Mach. Vis. Appl.*, vol. 27, no. 7, pp. 1103–1114, Oct. 2016, doi: 10.1007/s00138-016-0779-1.

[2] K. Patil, M. Kulkarni, A. Sriraman, and S. Karande, "Deep learning based car damage classification," in *Proc. 16th IEEE Int. Conf. Mach. Learn. Appl. (ICMLA)*, Dec. 2017, pp. 50–54.

[3] J. De Deijn, "Automatic car damage recognition using convolutional neural networks," M.S. thesis, Fac. Sci., Vrije Universiteit Amsterdam, Amsterdam, The Netherlands, 2018. [Online]. Available: https://science.vu.nl/en/Images/stageverslag-deijn_tcm296-882561.pdf

[4] S. Liu, D. Huang, and Y. Wang, "Receptive field block net for accurate and fast object detection," in *Proc. Eur. Conf. Comput. Vis.* Cham, Switzerland: Springer, 2018, pp. 404–419.

[5] T. Kaichi, S. Mori, H. Saito, J. Sugano, and H. Adachi, "Multi-view surface inspection using a rotating table," *Electron. Imag.*, vol. 30, no. 9, pp. 278-1–278-5, Jan. 2018.

[6] M. Seeland and P. Mäder, "Multi-view classification with convolutional neural networks," *PLoS ONE*, vol. 16, no. 1, Jan. 2021, Art. no. e0245230, doi: 10.1371/journal.pone.0245230.

[7] R. E. van Ruitenbeek and S. Bhulai, "Convolutional neural networks for vehicle damage detection," *Mach. Learn. Appl.*, vol. 9, Sep. 2022, Art. no. 100332. [Online]. Available: https://www.sciencedirect.com/science/article/pii/S2666827022000433?via%3Dihub

[8] S. Stent, R. Gherardi, B. Stenger, and R. Cipolla, "Detecting change for multi-view, long-term surface inspection," in *Proc. Brit. Mach. Vis. Assoc. Soc. Pattern Recognit.*, Dec. 2015, pp. 1–127.

[9] C. Tang, Y. Ling, X. Yang, W. Jin, and C. Zheng, "Multi-view object detection based on deep learning," *Appl. Sci.*, vol. 8, no. 9, p. 1423, Aug. 2018. [Online]. Available: http://www.mdpi.com/2076-3417/8/9/1423

[10] R. E. van Ruitenbeek and S. Bhulai, "Multi-view damage inspection using single-view damage projection," *Mach. Vis. Appl.*, vol. 33, no. 3, pp. 1–11, May 2022. [Online]. Available: https://link.springer.com/article/10.1007/s00138-022-01295-w

[11] A. Nassar, S. Lefevre, and J. D. Wegner, "Simultaneous multi-view instance detection with learned geometric soft-constraints," in *Proc. IEEE/CVF Int. Conf. Comput. Vis. (ICCV)*, Oct. 2019, pp. 6558–6567.

[12] A. Sesyuk, S. Ioannou, and M. Raspopoulos, "A survey of 3D indoor localization systems and technologies," *Sensors*, vol. 22, no. 23, p. 9380, Dec. 2022. [Online]. Available: https://typeset.io/papers/a-survey-of-3d-indoor-localization-systems-and-technologies-3ara23sq

[13] J. Farrell and M. Barth. (Dec. 2001). *Integration of GPS/INS and Magnetic Markers for Advanced Vehicle Control*. [Online]. Available: https://escholarship.org/uc/item/2n67583p

[14] Y. Byun and Y. Kim, "Localization based on magnetic markers for an all-wheel steering vehicle," *Sensors*, vol. 16, no. 12, p. 2015, Nov. 2016. [Online]. Available: https://www.mdpi.com/1424-8220/16/12/2015

[15] Y. S. Byun and R. G. Jeong, "Position estimation of vehicle based on magnetic marker: Time-division position correction," *Sensors*, vol. 21, no. 24, p. 8274, Dec. 2021. [Online]. Available: https://www.mdpi.com/1424-8220/21/24/8274

[16] T. Koike-Akino, P. Wang, M. Pajovic, H. Sun, and P. V. Orlik, "Fingerprinting-based indoor localization with commercial mmWave WiFi: A deep learning approach," *IEEE Access*, vol. 8, pp. 84879–84892, 2020.

[17] X. Wang, L. Gao, S. Mao, and S. Pandey, "CSI-based fingerprinting for indoor localization: A deep learning approach," *IEEE Trans. Veh. Technol.*, vol. 66, no. 1, pp. 763–776, Jan. 2017.

[18] Y. Du, T. Arslan, and A. Juri, "Camera-aided region-based magnetic field indoor positioning," in *Proc. Int. Conf. Indoor Positioning Indoor Navigat. (IPIN)*, Oct. 2016, pp. 1–7.

[19] S. Gansemer, S. Hakobyan, S. Püschel, and U. Großmann, "3D WLAN indoor positioning in multi-storey buildings," in *Proc. IEEE Int. Workshop Intell. Data Acquisition Adv. Comput. Syst., Technol. Appl.*, Sep. 2009, pp. 669–672.

[20] H. Plank, T. Egger, C. Steffan, C. Steger, G. Holweg, and N. Druml, "High-performance indoor positioning and pose estimation with time-of-flight 3D imaging," in *Proc. Int. Conf. Indoor Positioning Indoor Navigat. (IPIN)*, Sep. 2017, pp. 1–8. [Online]. Available: http://ieeexplore.ieee.org/document/8115878/

[21] F. Zafari, A. Gkelias, and K. K. Leung, "A survey of indoor localization systems and technologies," *IEEE Commun. Surveys Tuts.*, vol. 21, no. 3, pp. 2568–2599, 3rd Quart., 2019.

[22] J. Yang, H. Lee, and K. Moessner, "Multilateration localization based on singular value decomposition for 3D indoor positioning," in *Proc. Int. Conf. Indoor Positioning Indoor Navig.*, Alcala de Henares, Spain, Oct. 2016, pp. 1–8. [Online]. Available: http://ieeexplore.ieee.org/document/7743627/

[23] H. Hellmers, A. Eichhorn, A. Norrdine, and J. Blankenbach, "IMU/magnetometer based 3D indoor positioning for wheeled platforms in NLoS scenarios," in *Proc. Int. Conf. Indoor Positioning Indoor Navigat. (IPIN)*, Alcala de Henares, Spain, Oct. 2016, pp. 1–8. [Online]. Available: http://ieeexplore.ieee.org/document/7743655/

[24] A. Poulose, J. Kim, and D. S. Han, "A sensor fusion framework for indoor localization using smartphone sensors and Wi-Fi RSSI measurements," in *Proc. Appl. Sci.*, Jan. 2019, vol. 9, no. 20, p. 4379. [Online]. Available: https://www.mdpi.com/2076-3417/9/20/4379

[25] M. Barata and U. Nunes. (May 2024). *Data Fusion of Wheel Encoders and Magnetic Sensors for Autonomous Vehicles Navigation*. Urbano Nunes. [Online]. Available: https://www.academia.edu/18267801/Data_Fusion_of_wheel_encoders_and_magnetic_sensors_for_autonomous_vehicles_navigation

[26] L. Conde Bento and U. Nunes, "Autonomous navigation control with magnetic markers guidance of a cybernetic car using fuzzy logic," *J. Mach. Intell. Robot. Control*, vol. 6, pp. 1–10, Jun. 2004.

[27] R. Shirai, Y. Itoh, and M. Hashimoto, "Make it trackable: An instant magnetic tracking system with coil-free tiny trackers," *IEEE Access*, vol. 9, pp. 26616–26632, 2021. [Online]. Available: https://ieeexplore.ieee.org/document/9350270/

[28] X. T. Trinh, J.-T. Jeng, H.-T. Nguyen, V. S. Luong, and C.-C. Lu, "Two-dimensional position tracking using gradient magnetic fields," *Sensors*, vol. 22, no. 14, p. 5459, Jul. 2022. [Online]. Available: https://www.ncbi.nlm.nih.gov/pmc/articles/PMC9321341/

[29] M. J. Caruso and L. Withanawasam, "Vehicle detection and compass applications using amr magnetic sensors," Honeywell Aerospace, Plymouth, MN USA, Tech. Rep. 15533663, 1999. [Online]. Available: https://www.semanticscholar.org/paper/VEHICLE-DETECTION-AND-COMPASS-APPLICATIONS-USING-Caruso-Withanawasam/d33ceb08e031877602d3cd8d32576486718a2581

[30] Y. Wang, Q. Fu, and Y. Sui, "A robust tracking method for multiple moving targets based on equivalent magnetic force," *Micromachines*, vol. 13, no. 11, p. 2018, Nov. 2022. [Online]. Available: https://www.ncbi.nlm.nih.gov/pmc/articles/PMC9694121/

[31] J. Kim, W. Shin, H. Park, and J. Baek, "Addressing the occlusion problem in multi-camera people tracking with human pose estimation," in *Proc. IEEE/CVF Conf. Comput. Vis. Pattern Recognit. Workshops (CVPRW)*, Jun. 2023, pp. 5463–5469.

[32] A van den Hengel, R. Hill, B. Ward, A. Cichowski, H. Detmold, C. Madden, A. Dick, and J. Bastian, "Automatic camera placement for large scale surveillance networks," in *Proc. Workshop Appl. Comput. Vis.*, 2009, pp. 1–6.

[33] S. Fleishman, D. Cohen-Or, and D. Lischinski, "Automatic camera placement for image-based modeling," *Comput. Graph. Forum*, vol. 19, no. 2, pp. 101–110, Jun. 2000, doi: 10.1111/1467-8659.00447. [Online]. Available: http://doi.wiley.com/10.1111/1467-8659.00447

[34] T. Oki, R. Miyamoto, H. Yomo, and S. Hara, "Detection accuracy of soccer players in aerial images captured from several viewpoints," *J. Funct. Morphol. Kinesiol.*, vol. 4, no. 1, p. 9, Jan. 2019. [Online]. Available: https://www.mdpi.com/2411-5142/4/1/9

[35] A. Maglo, A. Orcesi, J. Denize, and Q. C. Pham, "Individual locating of soccer players from a single moving view," *Sensors*, vol. 23, no. 18, p. 7938, Sep. 2023. [Online]. Available: https://www.mdpi.com/1424-8220/23/18/7938

[36] S. Gerke, A. Linnemann, and K. Müller, "Soccer player recognition using spatial constellation features and Jersey number recognition," *Comput. Vis. Image Understand.*, vol. 159, pp. 105–115, Jun. 2017. [Online]. Available: https://linkinghub.elsevier.com/retrieve/pii/S1077314217300723

[37] A. Zaarane, I. Slimani, W. Al Okaishi, I. Atouf, and A. Hamdoun, "Distance measurement system for autonomous vehicles using stereo camera," *Array*, vol. 5, Mar. 2020, Art. no. 100016. [Online]. Available: https://www.sciencedirect.com/science/article/pii/S2590005620300011

[38] E. Dandil and K. K. Çevik, "Computer vision based distance measurement system using stereo camera view," in *Proc. 3rd Int. Symp. Multidisciplinary Stud. Innov. Technol. (ISMSIT)*, Oct. 2019, pp. 1–4.

[39] X. Shan, A. Cabani, and H. Chafouk, "A survey of vehicle localization: Performance analysis and challenges," *IEEE Access*, vol. 11, pp. 107085–107107, 2023.

[40] S.-H. Cha, "Comprehensive survey on distance/similarity measures between probability density functions," *Int. J. Math. Models Methods Appl. Sci.*, vol. 1, pp. 300–307, Jan. 2007. [Online]. Available: http://www.naun.org/main/NAUN/ijmmas/mmmas-49.pdf

[41] A. K. Jain, M. N. Murty, and P. J. Flynn, "Data clustering: A review," *ACM Comput. Surv.*, vol. 31, no. 3, pp. 264–323, Sep. 1999.

[42] A. Javed, B. S. Lee, and D. M. Rizzo, "A benchmark study on time series clustering," *Mach. Learn. Appl.*, vol. 1, Jan. 2020, Art. no. 100001. [Online]. Available: https://www.sciencedirect.com/science/article/pii/S2666827020300013

[43] K. M. Bergen, D. G. Brown, J. F. Rutherford, and E. J. Gustafson, "Change detection with heterogeneous data using ecoregional stratification, statistical summaries and a land allocation algorithm," *Remote Sens. Environ.*, vol. 97, no. 4, pp. 434–446, Sep. 2005.

[44] S. Lhermitte, J. Verbesselt, W. W. Verstraeten, and P. Coppin, "A comparison of time series similarity measures for classification and change detection of ecosystem dynamics," *Remote Sens. Environ.*, vol. 115, no. 12, pp. 3129–3152, Dec. 2011.

[45] C. Chen, Y. Wang, G. Huang, and H. Xiong, "Hierarchical demand forecasting for factory production of perishable goods," in *Proc. IEEE Int. Conf. Big Data (Big Data)*, Dec. 2019, pp. 188–193.

[46] T. Nakamura, K. Taki, H. Nomiya, K. Seki, and K. Uehara, "A shape-based similarity measure for time series data with ensemble learning," *Pattern Anal. Appl.*, vol. 16, no. 4, pp. 535–548, Nov. 2013.

[47] Bosch Sensortec GmbH. (2023). *BMM350 3-Axis Magnetic Sensor Datasheet*. Accessed: Aug. 10, 2025. [Online]. Available: https://www.bosch-sensortec.com/media/boschsensortec/downloads/datasheets/bst-bmm350-ds001.pdf

[48] Benewake (Beijing) Co. Ltd. (2024). *TFmini Plus Single-Point Ranging LiDAR Datasheet*. Accessed: Aug. 10, 2025. [Online]. Available: https://cdn.sparkfun.com/assets/1/4/2/1/9/TFmini_Plus_A02_Product_Manual_EN.pdf

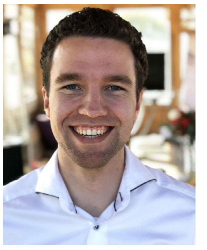

R. E. VAN RUITENBEEK was born in 1995. He received the B.S. and M.S. degrees (Hons.) in business analytics from the Vrije Universiteit Amsterdam, in 2017 and 2019, respectively. He is currently pursuing the Ph.D. degree in applied mathematics.

In 2017, he completed his secondary area of specialization in business, mathematics and information from The University of Manchester. From 2017 to 2021, he was an AI Engineer with Pon, to bring academic knowledge into practice. In 2022, he established Lensor, a company exclusively focused on the automation of vehicle damage assessment using computer vision. In 2020, he received the Business Analytics Best Paper Award for his research in the field of demand forecasting using hierarchical agglomeration clustering.

S. BHULAI was born in 1976. He received the M.Sc. degree in business mathematics and informatics and the Ph.D. degree in mathematics from Vrije Universiteit Amsterdam, The Netherlands. He is a Full Professor of business analytics with Vrije Universiteit Amsterdam. He has been a Postdoctoral Researcher with Lucent Technologies and Bell Laboratories and NWO Talent Stipend Fellow.